Comprehensive theoretical and experimental analysis of Coster-Kronig electron spectra from 64-MeV S^{12+} ions excited through He gas and C-foil targets

M. Sataka,[1] M. Imai,[2] K. Kawatsura,[3] K. Komaki,[4] H. Tawara,[5,6] A. Vasilyev,[7] and U. I. Safronova[1,7]
[1]*Department of Materials Science, Japan Atomic Energy Research Institute, Tokai, Ibaraki 319-1195, Japan*
[2]*Department of Nuclear Engineering, Kyoto University, Sakyo, Kyoto, 606-8501, Japan*
[3]*Department of Chemistry, Faculty of Engineering and Design, Kyoto Institute of Technology, Matsugasaki, Sakyo, Kyoto, 606-8585, Japan*
[4]*Institute of Physics, Graduate School of Art and Sciences, University of Tokyo, Meguro 153-8902, Japan*
[5]*Department of Physics, Kansas State University, Manhattan, Kansas 66506-2601*
[6]*Atomic Physics Division, National Institute of Standards and Technology, Gaithersburg, Maryland 20899-8421*
[7]*Department of Physics, University of Notre Dame, Notre Dame, Indiana 46556-5670*
(Received 25 November 2001; published 16 April 2002)

In Coster-Kronig electrons from the autoionizng Rydberg states of 64 MeV S^{12+} ions excited through He gas and very thin C-foil targets, several peaks have been observed in the electron energy range up to 2.5 eV. To obtain a better understanding on low-energy electron production mechanisms in such collisions, we synthesize the expected electron spectrum by assuming that the spectral (energy) distribution of each line can be expressed with a Gaussian profile with proper resolution and compare that with the observed spectrum. Two theoretical methods, namely, the perturbation theory of the *Z*-expansion (MZ code) and multiconfiguration Hartree-Fock method (Cowan code) are used to calculate Auger electron energies and rates. It is found that the $1s2p15l-1s2s\,^1S$, $1s2p13l-1s2s\,^3S$, $1s^22p9l-1s^22s$, $1s^22s2p9l-1s^22s^2$, $1s^22p^27l-1s^22s2p\,^3P$, and $1s^22p^29l-1s^22s2p\,^1P$ decays give a significant contribution in the electron spectrum near threshold in the range of 0–2.5 eV. Synthetic spectra have been found to reproduce the observed spectra reasonably well if the ion charge distributions are taken into account properly. Based upon the synthetic electron spectra from particular core configurations best fitted to the observed spectra, we have inferred the ion charge ''inside'' foils which can be compared with the well-established equilibrium charge ''after'' foil.

DOI: 10.1103/PhysRevA.65.052704 PACS number(s): 34.50.Fa, 82.80.Pv, 79.20.Rf, 32.80.Rm

I. INTRODUCTION

The present paper is a part of our continuing effort to study the Coster-Kronig electrons emitted from high-energy, highly charged ions colliding with gas and thin foil targets [1,2]. We had previously measured these electrons when the 64 MeV S^{q+} ($q=6,11,12,13$) ion passed through either He gas atoms or carbon foils. At first we tried to identify only the energy of the observed peaks by comparing the calculated values based upon the quantum-defect theory [3]. Furthermore, to identify the observed Auger electron peaks and compare the energy distribution (spectrum), the electron energy for the singlet and triplet $1s^22pnl(n=9–20)$ states of S^{12+} ions was calculated using the $1/Z$ expansion method [1] (see details later). It was pointed out that not only the primary four-electron ($1s^22p9l$) states but also three-electron ($1s2p13l$ and $1s2p15l$) states as well as the five-electron ($1s^22s2p9l$, $1s^22p^27l$ and $1s^22p^29l$) states had to be taken into account to reproduce the observed electron spectra from S^{12+} ion collisions [2].

In the present paper, we observe the electron spectrum from 65 MeV S^{12+} ions passing through He gas and carbon foil and furthermore perform more detailed calculations of the Auger electron energy and Auger rates for the following decays over the electron energy range of up to 2.6 eV to understand the electron emission mechanisms; $1s2p15l-1s2s\,^1S$, $1s2p13l-1s2s\,^3S$, $1s^22p9l-1s^22s$, $1s^22s2p9l-1s^22s^2$, $1s^22p^27l-1s^22s2p\,^{1,3}P$, and $1s^22p^29l-1s^22s2p\,^1P$. Two theoretical methods, namely, the perturbation theory of the *Z*-expansion (MZ code) [4,5] and multiconfiguration Hartree-Fock method (Cowan code) [6], are utilized to get the atomic data necessary for the present analysis. First, assuming the Gaussian (distribution) profile for each transition and summing up all the possible transitions, we synthesize the electron spectrum for each decay of ions with specific charge state ($q=11,12,13$). Then, combining these results with properly weighting factors for various decays of each charged ion, it is found that the final synthetic electron spectrum can reproduce nicely the observed spectrum. We also discuss and point out the relevance of the observed electron spectrum to the ion charge distributions inside foils.

II. EXPERIMENT

The present experimental apparatus has been described in detail [7], and only a brief description is given here. The zero-degree electron spectroscopy technique was applied to measure the electrons ejected from projectile ions. S^{6+} ions were accelerated with the tandem accelerator of the Japan Atomic Energy Research Institute, Tokai, and poststripped through a carbon foil of 10 $\mu g/cm^2$ and, then, the ions of the required charge state were selected with a magnet. The projectile ions were collimated to a diameter of 2 mm, and col-

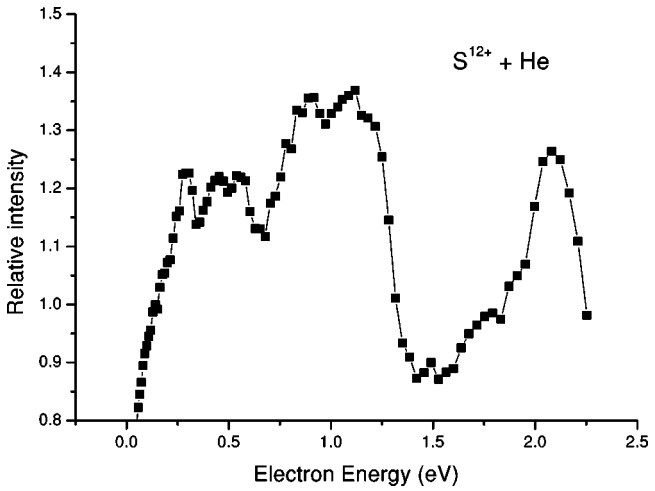

FIG. 1. Experimental Coster-Kronig electron spectrum of sulfur ions. The electron energy is in the projectile frame.

lected in a Faraday cup after collisions with He gas or carbon foil with a thickness of 2.2 μg/cm^2 to integrate the total number of ions. The electrons ejected into the ion-beam direction were measured with a tandem 45° parallel plate electron spectrometer. To get better energy resolution, the second analyzer was set to pass only 50 eV electrons through, and, thus, electron spectra in the laboratory frame were obtained by scanning a retarding potential between the first and second analyzers. The electron spectra transformed into the projectile frame through Lorenz transformation are shown in Fig. 1 (He gas) and Fig. 2 (2.2 μg/cm^2 carbon foil).

III. THEORETICAL TECHNIQUE

In Table I we present absolute energy (E) and ionization potential (I) for different stage of ionization of sulfur ions calculated using MZ code. MZ code was based on the perturbation theory method with Coulomb basis. This method was described in detail by Safronova and Senashenko [4] and Safronova *et al.* [5]. In this method ($1/Z$ method or $1/Z$ expansion method) the energy matrix is represented in the form

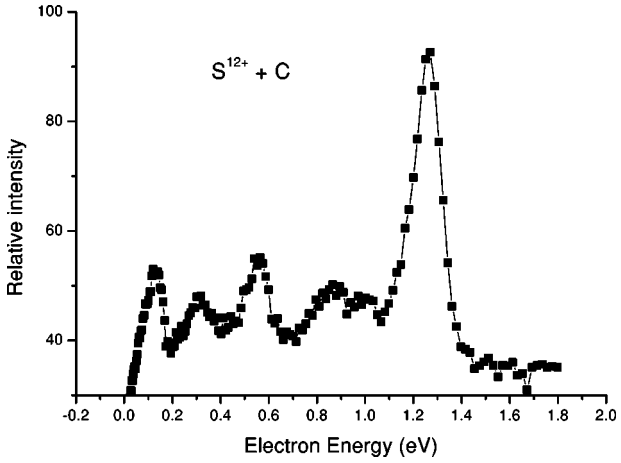

FIG. 2. Experimental Coster-Kronig electron spectrum of sulfur ions. The electron energy is in the projectile frame.

of $1/Z$-expansion series (Z is the nuclear charge) and the calculation of every coefficient of this series is carried out by means of the Feynman diagram technique. An advantage of this method is that the coefficients are constant for the whole isoelectronic sequence and depend only on the electronic state. We note that mixing of configurations inside one complex is taken into account by the first-order coefficients of the series. The complex of states means a group of configurations with the same parity and the same set of the principal quantum numbers ($1s^22s^22p+1s^22p^3$, for example). The mixing between configurations of different complexes is taken into account with the second- and higher-order diagrams of the perturbation theory method. The Breit operators are responsible for the relativistic contribution. The radiative corrections (Lamb shift) and high-order relativistic contributions are also taken into account in MZ code. We will not discuss calculation of all $1/Z$ coefficients in detail here (see [4,5] for details).

In Table II we list and compare the Auger electron energies of the $1s2pnl$ Rydberg states with $n=13$ and 15 for S^{13+} calculated using MZ and Cowan codes. It should be noted that the atomic structure code of Cowan [6] enables us to get results which are generally in good agreement with experimental energies by scaling the electrostatic Slater parameters to include the correlation effects (Pindzola *et al.* [8]). We use the scaling factor of 0.92 in the present paper. It can be seen from this Table that the discrepancy between two methods is about 0.1–0.4 eV. The Auger electron energies of $1s2p15l$ and $1s2p13l$ states are measured from the $1s2s\,^1S_0$ and $1s2s\,^3S_1$ thresholds, respectively. We can see from Table I that, in order to obtain the accuracy of 0.1–0.4 eV, we need to calculate absolute values of both the upper and lower states with the accuracy of 0.002–0.01 %. This is the main problem of calculations of the Auger electron energies near threshold. Using Cowan code, we mix the doubly excited $1s2pnl$ states with the excited $1s^2nl$ states. As a result, we calculate the energy E^d of the doubly excited $1s2pnl$ states relative to the ground $1s^22s\,^2S_{1/2}$ state. Then, we obtain the Auger electron energy as the difference between E^d and ionization potential I listed in Table I. We present the ionization potential for $1s^22s\,^2S_{1/2}$, $1s^2\,^1S_0$, $1s2s\,^1S_0$, and $1s2s\,^3S_1$. The last two values are used to calculate the Auger electron energy for $1s2p15l$ and $1s2p13l$ states, respectively.

It should be noted that the atomic structure code of Cowan allows us to mix about 50 $1s2lnl'$ configurations. We choose the following configurations with even and odd parity to obtain results presented in Table II.

Even-parity states: $1s^22s$, $1s^23s$, $1s2s^2$, $1s2p^2$, $1s2s3s$, $1s2s3d$, $1s2p3p$, $1s2s4s$, $1s2s4d$, $1s2p4p$, $1s2p4f$, $1s2s5s$, $1s2s5d$, $1s2s5g$, $1s2p5p$, $1s2p5f$, $1s2snl$, with $n=9$, 10, 15, and $l=s,d,g,i$; $1s2pnl$, with $n=9$, 10, 15, and $l=p,f,h,k$; $1s2p10m$, $1s2p15m$.

Odd-parity states: $1s^22p$, $1s^23p$, $1s2s2p$, $1s2s3p$, $1s2p3s$, $1s2p3d$, $1s2s4p$, $1s2s4f$, $1s2p4s$, $1s2p4d$,$1s2s5p$, $1s2s5f$, $1s2p5s$, $1s2p5d$, $1s2p5g$, $1s2snl$, with $n=9,10,15$, and $l=p,f,h,k$; $1s2s10m$, $1s2s15m$; $1s2pnl$, with $n=9,10,15$, and $l=s,d,g,i$.

The most important mixing occurs between states with the

TABLE I. Absolute values of energy (E) and ionization potential (I) for different configurations of $S^{14+}-S^{11+}$ ions in units of 10^3 cm^{-1} calculated with the MZ code.

Configurations	LSJ	E	Configurations	LSJ	E
$1s2s$	$^1S_0$	34438.530	$1s^22p^2$	$^3P_0$	64623.730
$1s2s$	$^3S_1$	34581.920	$1s^22p^2$	$^3P_1$	64618.100
$1s2p$	$^1P_1$	34337.640	$1s^22p^2$	$^3P_2$	64610.000
$1s2p$	$^3P_0$	34449.750	$1s^22p^2$	$^1D_2$	64557.310
$1s2p$	$^3P_1$	34446.490	$1s^22p^2$	$^1S_0$	64424.900
$1s2p$	$^3P_2$	34433.420	$1s^22s2p$	$^1P_1$	64757.370
$1s^2$	$^1S_0$	54184.010	$1s^22s2p$	$^3P_0$	64947.670
$1s^22s$	$^2S_{1/2}$	59886.450	$1s^22s2p$	$^3P_1$	64943.340
$1s^22p$	$^2P_{1/2}$	59646.980	$1s^22s2p$	$^3P_2$	64933.490
$1s^22p$	$^2P_{3/2}$	59662.160	$1s^22s^22p$	$^2P_{1/2}$	69697.320
$1s^22s^2$	$^1S_0$	65147.070	$1s^22s^22p$	$^2P_{3/2}$	69684.032
Configurations	LSJ		Configurations	LSJ	I
$1s^22s$	$^2S_{1/2}$		$1s^2$	$^1S_0$	5702.44
$1s^22s$	$^2S_{1/2}$		$1s2s$	$^1S_0$	25447.92
$1s^22s$	$^2S_{1/2}$		$1s2s$	$^3S_1$	25304.53
$1s^22s^2$	$^1S_0$		$1s^22s$	$^2S_{1/2}$	5260.62
$1s^22s^22p$	$^2P_{1/2}$		$1s^22s^2$	$^1S_0$	4550.25
$1s^22s^22p$	$^2P_{1/2}$		$1s^22s2p$	$^3P_0$	4749.65
$1s^22s^22p$	$^2P_{1/2}$		$1s^22s2p$	$^3P_1$	4753.98
$1s^22s^22p$	$^2P_{1/2}$		$1s^22s2p$	$^3P_2$	4763.83
$1s^22s^22p$	$^2P_{1/2}$		$1s^22s2p$	$^1P_1$	4939.95

same principal quantum numbers ($1s2s3p$, $1s2p3s$, and $1s2p3d$, for example). We examined the influence of the scaling parameters on our energy-level calculations and found that different scaling parameters change the level energy up to 0.1 to 0.2 eV. This agrees with the previous conclusion [9].

TABLE II. Comparison of Auger electron energies (in eV) for S^{13+} calculated using Cowan (a) and MZ (b) codes.

1s2pnl LSJ	E^a	E^b	1s2pnl LSJ	E^a	E^b
$15s\ ^2P_{1/2}$	0.7532	0.6646	$13s\ ^4P_{1/2}$	0.7510	0.6659
$15s\ ^2P_{3/2}$	0.7544	0.6658	$13p\ ^4D_{1/2}$	0.7201	0.7329
$15p\ ^2D_{3/2}$	0.8012	0.7389	$13p\ ^4D_{3/2}$	0.8372	0.7527
$15p\ ^2P_{1/2}$	0.8028	0.7501	$13d\ ^4F_{3/2}$	0.8879	0.8073
$15p\ ^2D_{5/2}$	0.8043	0.7414	$13d\ ^4D_{5/2}$	0.9015	0.8222
$15p\ ^2P_{3/2}$	0.8078	0.7538	$13f\ ^4G_{5/2}$	0.9228	0.8482
$15p\ ^2S_{1/2}$	0.8204	0.7340	$13f\ ^4F_{7/2}$	0.9259	0.8519
$15d\ ^2D_{5/2}$	0.8448	0.7910	$13s\ ^4P_{3/2}$	1.4360	1.0528
$15d\ ^2F_{7/2}$	0.8448	0.8059	$13s\ ^2P_{1/2}$	1.4769	1.0850
$15d\ ^2F_{5/2}$	0.8476	0.7935	$13p\ ^4D_{3/2}$	1.5072	1.0924
$15f\ ^2F_{5/2}$	0.8578	0.8233	$13p\ ^4D_{5/2}$	1.5223	1.1172
$15f\ ^2F_{7/2}$	0.8585	0.8233	$13p\ ^4P_{1/2}$	1.5284	1.1334
$15d\ ^2P_{1/2}$	0.8600	0.7811	$13p\ ^4D_{1/2}$	1.5472	1.1470
$15d\ ^2P_{3/2}$	0.8627	0.7848	$13p\ ^2D_{3/2}$	1.5529	1.1482
$15f\ ^2G_{7/2}$	0.8681	0.8282	$13d\ ^4F_{5/2}$	1.5759	1.1594
$15f\ ^2D_{3/2}$	0.8752	0.7985	$13d\ ^4D_{3/2}$	1.5901	1.1792
$15f\ ^2D_{5/2}$	0.8763	0.7997	$13d\ ^4F_{7/2}$	1.5911	1.1805

Let us discuss some details on calculation using MZ code for Rydberg states such as $1s2l'nl$ states. We have already mentioned that MZ code is based on the representation of every atomic characteristics in the form of $1/Z$ expansion. For the $1s2l'nl$ states, it is convenient to divide the value of each ith order $E^{(i)}$ coefficient into two parts, namely, the core and Rydberg parts

$$E^{(i)}(1s2l'nl)=E^{(i)}(1s2l')+E^{(i)}(nl). \tag{3.1}$$

The two-electron core term, $E^{(i)}(1s2l')$, is calculated as we explained previously (see [4,5]).

Let us consider the asymptotic behavior of the second term. The first- and second-order nonrelativistic terms in $1/Z$ expansion $[E_N^{(1)}(nl)$ and $E_N^{(2)}(nl)]$ include the $1/n^2$ term as a leading term

$$E_N^{(1)}(nl)=\frac{2}{n^2}+E_1'(nl), \quad E_N^{(2)}(nl)=-\frac{2}{n^2}+E_2'(nl). \tag{3.2}$$

The first terms in Eq. (3.2) give the largest contribution to the value of each coefficient in $E_N^{(1)}(nl)$ and $E_N^{(2)}(nl)$. The second terms $E_1'(nl)$ and $E_2'(nl)$ are proportional to $1/n^3$

$$E_1'(nl)=\frac{\varepsilon_1}{n^3}, \quad E_2'(nl)=\frac{\varepsilon_2}{n^3}. \tag{3.3}$$

TABLE III. The Auger energies (E_S) in eV, weighted sum of transition probabilities (gA_r), and autoionization rates (A_a) in units of 10^{13} s^{-1} for Li-like S^{13+} ions.

$nl\,LSJ$	E_S	gA_r	A_a	LSJ	E_S	gA_r	A_a
$[1s2p(^1P)nl\,LSJ-1s2s\,^1S_0]$ decay				$[1s2p(^3P)nl\,LSJ-1s2s\,^3S_1]$ decay			
$15s\,^2P_{1/2}$	0.7532	0.0057	0.2509	$13s\,^4P_{1/2}$	0.7510	0.0075	0.4316
$15s\,^2P_{3/2}$	0.7544	0.0140	0.2188	$13p\,^4D_{1/2}$	0.8201	0.0357	0.3257
$15p\,^2D_{3/2}$	0.8012	0.0698	0.1056	$13s\,^4P_{3/2}$	1.4360	0.0121	0.3260
$15p\,^2D_{5/2}$	0.8043	0.1140	0.1073	$13s\,^2P_{1/2}$	1.4769	0.0238	0.3575
$15p\,^2S_{1/2}$	0.8204	0.0308	1.2983	$13p\,^4D_{3/2}$	1.5072	0.0501	0.3270
$15d\,^2P_{1/2}$	0.8600	0.0147	0.3986	$13p\,^4D_{1/2}$	1.5472	0.0805	0.9364
$15d\,^2P_{3/2}$	0.8627	0.0286	0.4006	$13p\,^2D_{3/2}$	1.5529	0.1408	0.3664
$15f\,^2G_{9/2}$	0.8679	0.0108	0.1244	$13s\,^2P_{3/2}$	3.1624	0.0386	1.0388
$15f\,^2G_{7/2}$	0.8681	0.0109	0.1263	$13p\,^4P_{3/2}$	3.2092	0.0384	0.4297
$15g\,^2H_{9/2}$	0.8735	0.0039	0.1690	$13p\,^2P_{3/2}$	3.2175	0.1181	0.4982
$15g\,^2H_{11/2}$	0.8737	0.0045	0.1688	$13p\,^2S_{1/2}$	3.2629	0.1022	1.4938
$15h\,^2I_{11/2}$	0.8764	0.0019	0.1768	$13d\,^4P_{1/2}$	3.2896	0.0079	0.4935
$15h\,^2I_{13/2}$	0.8767	0.0022	0.1768	$13d\,^4P_{3/2}$	3.2911	0.0337	0.3980
$15i\,^2K_{13/2}$	0.8786	0.0012	0.1673	$13g\,^4H_{13/2}$	3.3209	0.0080	0.3151
$15i\,^2K_{15/2}$	0.8787	0.0014	0.1673	$13g\,^2H_{11/2}$	3.3213	0.0081	0.3192
$15k\,^2L_{15/2}$	0.8793	0.0013	0.1442	$13h\,^2I_{13/2}$	3.3232	0.0038	0.3194
$15k\,^2L_{17/2}$	0.8793	0.0014	0.1441	$13h\,^4I_{15/2}$	3.3235	0.0043	0.3192
$15l\,^2M_{17/2}$	0.8793	0.0011	0.1116	$13i\,^2K_{15/2}$	3.3250	0.0026	0.2845
$15l\,^2M_{19/2}$	0.8794	0.0012	0.1116	$13i\,^4K_{17/2}$	3.3252	0.0029	0.2845

First, we calculate the $E^{(i)}(1s2l'nl)$ coefficient for $n=n_0(n_0=3,4)$ using Feynman diagram technique. Then, we subtract the $E^{(i)}(1s2l')$ [Eq. (3.1)] value and the leading $2/n^2$ [Eq. (3.2)] terms from the calculated $E^{(i)}(1s2l'nl)$ and, as a result, we obtain the values of ε_1 and ε_2 terms. Then, these coefficients are used to calculate $E_N^{(1)}(nl)$ and $E_N^{(2)}(nl)$ for $n=13$ and 15 using Eqs. (3.3) and (3.2). Here, we explained only the calculation of the diagonal matrix elements for the nonrelativistic part of energy [Eq. (3.1)]. Similar formulas are used to calculate the coefficients describing the relativistic part of energy as well as the nondiagonal matrix elements (see [10] for details). Results of our calculations using MZ code are presented and compared with those of Cowan code in Table II.

It can be seen from this table that Auger electron energy for $1s2p13l$ and $1s2p15l$ states calculated both by Cowan code including the 45 odd-parity and 46 even-parity states and by MZ code including the asymptotic representations is in good agreement with each other. This indicates high accuracy of the present calculations in both methods and this is very important in precise identification of electron spectra near threshold region.

IV. AUGER ELECTRON ENERGIES AND RATES FOR LI-, BE-, AND B-LIKE SULFUR IONS

We calculate Auger electron energies, radiative and autoionization rates for the $1s2p15l$, $1s2p13l$, $1s^22p9l$, $1s^22s2p9l$, $1s^22p^27l$, and $1s^22p^29l$ Rydberg states in sulfur ions with various charge. Our results are listed in Tables III–VI.

In Table III we present the $[1s2p(^1P)15l\,LSJ-1s2s\,^1S_0]$ and $[1s2p(^3P)13l\,LSJ-1s2s\,^3S_1]$ Auger electron energies (E_S) in units of eV, weighted sum of radiative rates (gA_r) and autoionization rates (A_a) in units of 10^{13} s^{-1} for Li-like S^{13+} ions. We already explained in the previous paragraph that Auger electron energy is obtained as the difference between two absolute energies. The radiative rates for $1s2p(^1P)15l\,LSJ$ and $1s2p(^3P)13l\,LSJ$ states are computed as a sum of radiative transition probabilities from these states in all lower states. The radiative rates for the $1s2pnl$ states with $l=s,d,g,i$ are calculated by choosing the lower states among the 46 even-parity configurations and for the $1s2pnl$ states with $l=p$, f, h, k, and m among the 45 odd-parity configurations. The autoionization rates, A_a, are calculated as the square of amplitude of the $[1s2p(^1P)15l\,LSJ-1s2s\,^1S_0]$ and $[1s2p(^3P)13l\,LSJ-1s2s\,^3S_1]$ decays, respectively. In Table III we list the $1s2p(^1P)15l\,LSJ$ and $1s2p(^3P)13l\,LSJ$ states with A_a larger than 0.1 in 10^{13} s^{-1} units.

In Table IV Auger electron energies, weighted sum of transition probabilities (gA_r) and autoionization rates (A_a) from the $[1s^22pnl\,LSJ-1s^22s]$ states are presented for Be-like S^{12+} ions. The present data differ slightly from data previously given in [1]. This difference is due to the different scaling factor used in the present and the previous [1] papers. We used here the scaling factor of 0.92, meanwhile the scaling factor of 0.85 was used in [1]. We examine different scaling factors by comparison with experimental energy levels for the low-lying levels in Be-like S^{12+} ions. Indeed we found that the scaling factor of 0.92 better reproduces the

TABLE IV. The $[1s^2 2pnl\,LSJ - 1s^2 2s]$ Auger energies (E_S) in eV, weighted sum of transition probabilities (gA_r), and autoionization rates (A_a) in units of 10^{13} s^{-1} for Be-like S^{12+} ions.

$nl\,LSJ$	E_S	gA_r	A_a	LSJ	E_S	gA_r	A_a
$9s\,^3P_2$	0.7897	0.0125	0.3013	$9h\,^1H_5$	1.4670	0.0170	0.3297
$9s\,^1P_1$	0.8327	0.0134	3.2076	$9h\,^3H_6$	1.4680	0.0201	0.3303
$9p\,^1P_1$	1.0888	0.0291	0.3221	$9h\,^3H_4$	1.4718	0.0141	0.0061
$9p\,^3D_3$	1.1006	0.0300	0.1455	$9g\,^3H_6$	1.4719	0.0293	1.4343
$9p\,^3S_1$	1.1500	0.0191	2.3490	$9f\,^1G_4$	1.4728	0.0370	1.4275
$9p\,^1D_2$	1.2234	0.0278	0.2149	$9g\,^1H_5$	1.4728	0.0249	1.4489
$9d\,^3F_4$	1.3042	0.0261	0.1162	$9d\,^1F_3$	1.4733	0.1010	1.0681
$9d\,^1D_2$	1.3108	0.0292	0.1175	$9i\,^1I_6$	1.4776	0.0146	0.2126
$9p\,^1S_0$	1.3647	0.0029	8.0012	$9i\,^3I_7$	1.4783	0.0169	0.2130
$9d\,^3D_2$	1.3770	0.0491	0.6881	$9h\,^1I_6$	1.4805	0.0198	1.1721
$9d\,^3P_1$	1.3852	0.0286	1.0653	$9h\,^3I_7$	1.4814	0.0228	1.1715
$9d\,^3P_0$	1.3905	0.0087	1.4506	$9i\,^1K_7$	1.4857	0.0166	0.7390
$9f\,^1F_3$	1.4155	0.0259	0.3060	$9i\,^3K_8$	1.4864	0.0188	0.7391
$9f\,^3F_4$	1.4238	0.0340	0.3841	$9k\,^1L_8$	1.4867	0.0145	0.3239
$9f\,^3G_5$	1.4434	0.0393	1.2019	$9k\,^3L_9$	1.4873	0.0162	0.3239
$9g\,^1G_4$	1.4480	0.0204	0.3910	$9g\,^3F_3$	1.4882	0.0234	0.2182
$9g\,^3G_5$	1.4500	0.0249	0.3979	$9d\,^1P_1$	1.4961	0.0413	1.0713

low-lying experimental energy than the scaling factor of 0.85. We already mentioned in the previous paragraph that we can obtain the difference in energy levels by about 0.1 eV when the scaling factor was changed in Cowan code. Comparison of our Auger electron energies presented in Table IV and in Table III [1] confirms our conclusion.

In Tables V and VI we list similar results for different decays in B-like S^{11+} ions. The $[1s^2 2s2p(^3P)9l\,LSJ - 1s^2 2s^2\,^1S]$ decay data are presented in Table V. It can be seen from this Table that A_a values are very small, compared with those for Be-like S^{12+} ions. The nearest $1s^2 2s2p \times (^3P)9l\,LSJ$ levels to the threshold $1s^2 2s^2\,^1S$ levels happen to be the quartet levels. The nonzero A_a for these levels are due to the relativistic effects which are still not so important for B-like S^{11+} ions. As a result, the largest A_a for the states considered are smaller by a factor of 10 than those for the LS-allowed decays in Be-like S^{12+} ions presented in Table IV. For the $1s^2 2s2p(^3P)9l\,LSJ$ states the radiative rates, gA_r, are larger than the autoionization rates, A_a, in many cases as can be seen from Table V.

The Auger electron energies, weighted sum of radiative rates, and autoionization rates for the $1s^2 2p^2(L_{12}S_{12})nl$ states are presented in Table VI. For these states, there are two possible thresholds for Coster-Kronig transitions: $1s^2 2s2p\,^1P$ and $1s^2 2s2p\,^3P$. The value of n when the $1s^2 2p^2(L_{12}S_{12})nl$ states become autoionizing depends on the intermediate term $L_{12}S_{12}$ and the threshold considered. The states with the singlet intermediate term, $1s^2 2p^2(^1D)nl$ and $1s^2 2p^2(^1S)nl$, relative to the $1s^2 2s2p\,^1P$ threshold become autoionizing for $n=9$ and $n=7$, respectively. The states with the triplet intermediate term, $1s^2 2p^2(^3P)nl$, relative to the $2s2p\,^3P$ threshold become autoionizing for $n=7$. We can also consider cases with $1s^2 2s2p\,^3P$ threshold for the $1s^2 2p^2(^1D)nl$ and $1s^2 2p^2(^1S)nl$ states and $1s^2 2s2p\,^1P$ threshold for the $1s^2 2p^2(^3P)nl$ states but the A_a for those decays should be much smaller than for previ-

TABLE V. The $[1s^2 2s2p(^3P)nl\,LSJ - 1s^2 2s^2\,^1S]$ Auger energies (E_S) in eV, weighted sum of transition probabilities (gA_r), and autoionization rates (A_a) in units of 10^{13} s^{-1} for B-like S^{11+} ions.

$nl\,LSJ$	E_S	gA_r	A_a	LSJ	E_S	gA_r	A_a
$9s\,^4P_{1/2}$	0.1402	0.0044	0.2200	$9d\,^2F_{5/2}$	1.4941	0.0611	0.1315
$9p\,^4D_{1/2}$	0.5090	0.0074	0.0146	$9f\,^2D_{5/2}$	1.5810	0.0196	0.0320
$9s\,^4P_{3/2}$	0.6801	0.0087	0.1607	$9s\,^2P_{3/2}$	1.9713	0.0132	0.7666
$9s\,^2P_{1/2}$	0.7491	0.0061	0.5807	$9p\,^2S_{1/2}$	2.4199	0.0151	0.1108
$9d\,^4D_{5/2}$	0.8674	0.0439	0.0459	$9d\,^2D_{5/2}$	2.6462	0.0431	0.0487
$9f\,^4G_{5/2}$	1.0013	0.0168	0.0113	$9d\,^2F_{7/2}$	2.7373	0.0937	0.2106
$9p\,^4D_{1/2}$	1.1337	0.0088	0.0716	$9f\,^2F_{5/2}$	2.7875	0.0212	0.0250
$9d\,^4F_{7/2}$	1.3931	0.0479	0.0427	$9f\,^2D_{3/2}$	2.8170	0.0158	0.0580

TABLE VI. The Auger energies (E_S) in eV, weighted sum of transition probabilities (gA_r), and autoionization rates (A_a) in units of 10^{13} s^{-1} for B-like S^{11+} ions.

$nl\,LSJ$	E_S	gA_r	A_a	LSJ	E_S	gA_r	A_a
$[1s^2 2p^2(^1D)nl\,LSJ - 1s^2 2s2p\,^1P]$ decay							
$9s\,^2D_{5/2}$	0.3577	0.0148	1.5739	$9f\,^2H_{9/2}$	1.2024	0.0225	2.2945
$9s\,^2D_{3/2}$	0.3582	0.0104	1.4980	$9f\,^2H_{11/2}$	1.2036	0.0266	2.3019
$9p\,^2P_{1/2}$	0.7935	0.0201	4.8243	$9i\,^2I_{11/2}$	1.2266	0.0024	2.4382
$9p\,^2P_{3/2}$	0.8131	0.0317	4.6665	$9g\,^2I_{13/2}$	1.2281	0.0176	2.4435
$9d\,^2D_{3/2}$	1.0692	0.0322	1.0800	$9h\,^2K_{13/2}$	1.2341	0.0083	1.9340
$9d\,^2P_{1/2}$	1.1206	0.0245	1.9512	$9h\,^2K_{15/2}$	1.2348	0.0095	1.9341
$9d\,^2P_{3/2}$	1.1430	0.0560	1.9344	$9i\,^2L_{15/2}$	1.2377	0.0033	1.1736
$9d\,^2S_{1/2}$	1.1543	0.0157	2.7448	$9i\,^2L_{17/2}$	1.2382	0.0037	1.1737
$[1s^2 2p^2(^1S)nl\,LSJ - 1s^2 2s2p\,^1P]$ decay							
$7f\,^2F_{5/2}$	0.2506	0.0450	5.5691	$7h\,^2H_{9/2}$	0.3265	0.0367	2.4796
$7f\,^2F_{7/2}$	0.2526	0.0600	5.5388	$7h\,^2H_{11/2}$	0.3279	0.0441	2.4796
$7g\,^2G_{7/2}$	0.2977	0.0387	4.5727	$7i\,^2I_{11/2}$	0.3391	0.0317	0.6991
$7g\,^2G_{9/2}$	0.2998	0.0484	4.5726	$7i\,^2I_{13/2}$	0.3402	0.0370	0.6990
$[1s^2 2p^2(^3P)nl\,LSJ - 1s^2 2s2p\,^3P_0]$ decay							
$7p\,^2S_{1/2}$	0.0321	0.0185	1.5943	$7f\,^4D_{7/2}$	0.4580	0.0480	2.9646
$7d\,^4F_{3/2}$	0.0987	0.0291	1.6297	$7s\,^2P_{3/2}$	0.5004	0.0232	8.8147
$7p\,^4D_{5/2}$	0.1188	0.0436	1.2535	$7g\,^4H_{7/2}$	0.5009	0.0266	2.4674
$7d\,^4F_{5/2}$	0.1694	0.0706	1.9495	$7g\,^4F_{9/2}$	0.5037	0.0332	2.4626
$7p\,^4D_{3/2}$	0.1749	0.0273	1.9878	$7h\,^4I_{9/2}$	0.5305	0.0218	1.3452
$7p\,^4P_{1/2}$	0.2728	0.0177	5.1897	$7h\,^4G_{11/2}$	0.5320	0.0261	1.3451
$7p\,^2D_{3/2}$	0.3067	0.0357	1.3502	$7p\,^2P_{1/2}$	1.2894	0.0182	1.2719
$7f\,^4G_{5/2}$	0.4430	0.0364	2.8734	$7p\,^2P_{3/2}$	1.4607	0.0330	1.6557
$[1s^2 2p^2(^3P)nl\,LSJ - 1s^2 2s2p\,^3P_1]$ decay							
$7d\,^4D_{1/2}$	0.2508	0.0140	1.7864	$7f\,^2G_{7/2}$	0.6308	0.0476	2.9753
$7d\,^2D_{3/2}$	0.4514	0.0592	2.0801	$7f\,^2F_{5/2}$	0.6507	0.0363	1.5742
$7d\,^2F_{5/2}$	0.4890	0.1321	2.8718	$7g\,^4H_{9/2}$	0.6612	0.0331	2.5421
$7f\,^4G_{9/2}$	0.5991	0.0605	2.8672	$7g\,^4H_{11/2}$	0.6615	0.0399	2.5279
$7p\,^4P_{5/2}$	0.6073	0.0458	2.0292	$7p\,^2P_{1/2}$	0.7526	0.0182	3.8157
$7f\,^4F_{3/2}$	0.6173	0.0247	1.5623	$7p\,^2P_{3/2}$	0.9238	0.0330	4.9671
$[1s^2 2p^2(^3P)nl\,LSJ - 1s^2 2s2p\,^3P_2]$ decay							
$7d\,^4D_{7/2}$	0.0377	0.0383	1.0743	$7g\,^2H_{11/2}$	0.4778	0.0398	1.9961
$7d\,^4D_{5/2}$	0.1022	0.0618	1.1554	$7f\,^2F_{5/2}$	0.4944	0.0364	1.3546
$7d\,^2F_{7/2}$	0.3408	0.1838	2.1694	$7g\,^4G_{9/2}$	0.5087	0.0332	1.4922
$7d\,^2D_{3/2}$	0.3412	0.0767	2.0156	$7g\,^2G_{7/2}$	0.5097	0.0265	1.2842
$7f\,^4G_{11/2}$	0.3927	0.0721	2.1811	$7g\,^4G_{11/2}$	0.5112	0.0398	1.7671
$7d\,^2D_{5/2}$	0.4462	0.1368	2.5939	$7h\,^2I_{13/2}$	0.5116	0.0305	1.0932
$7f\,^4F_{7/2}$	0.4519	0.0492	1.5139	$7h\,^4I_{15/2}$	0.5130	0.0348	1.0928
$7f\,^4F_{9/2}$	0.4735	0.0600	2.1846	$7g\,^2G_{9/2}$	0.5137	0.0330	1.5751
$7g\,^4H_{13/2}$	0.4772	0.0466	1.9837	$7f\,^2F_{7/2}$	0.5209	0.0378	1.4100

ous ones. In the first case, $[1s^2 2p^2(^1D)nl - 1s^2 2s2p\,^1P]$ and $[1s^2 2p^2(^1S)nl - 1s^2 2s2p\,^1P]$ decays are LS allowed, meanwhile in the second case, $[1s^2 2p^2(^1D)nl - 1s^2 2s2p\,^3P]$ and $[1s^2 2p^2(^1S)nl - 1s^2 2s2p\,^3P]$ decays are LS forbidden.

Our results for the $1s^2 2p^2(L_{12}S_{12})7l\,LSJ$ states with the triplet intermediate term and the triplet term for the threshold are also given in Table VI. We consider results relative to the $1s^2 2s2p\,^3P_0$, $1s^2 2s2p\,^3P_1$, and $1s^2 2s2p\,^3P_2$ thresholds. The multiplet splitting for $1s^2 2s2p\,^3P$ term is equal to 0.54

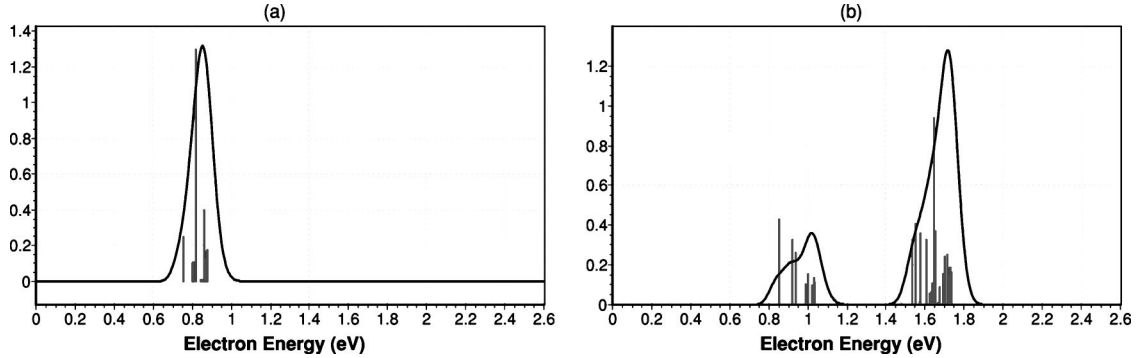

FIG. 3. Synthetic spectrum of S^{13+} with a resolution of 0.1 eV: (a) $[1s2p(^1P)15l-1s2s\ ^1S]$ decay; and (b) $[1s2p(^3P)13l-1s2s\ ^3S]$ decay. The scale in the ordinate is in units of $10^{13}\ s^{-1}$.

and 1.22 eV. Such shifts in threshold energy lead to the different l distributions in Auger electron energies, as can be seen from a comparison of the results in Table VI.

V. SYNTHETIC SPECTRA FOR LI-, BE-, AND B-LIKE SULFUR IONS

To create the synthetic Coster-Kronig electron spectrum, first we use the calculated Auger electron energies E_S and the autoionization rates A_a. It is assumed that the spectral (energy) distribution $I_n(E)$ of each nth transition has a Gaussian profile with the energy resolution of δE_n

$$I_n(E)=I(E_S^n)2\sqrt{\frac{\ln 2}{\pi}}\frac{1}{\delta E_n}\exp\left[-4\ln 2\left(\frac{E-E_S^n}{\delta E_n}\right)^2\right]. \tag{5.1}$$

Here, $\delta_n E$ and E_S^n are the linewidth (energy resolution) and the line energy position, respectively, and $I(E_S^n)=A_a^n$. By summing up the Gaussian profiles for all the possible N transition lines the synthetic spectrum can be obtained. The final synthetic spectrum can be expressed as a function of energy (E) in the following form:

$$I_S(E)=A\sum_{n=1}^{N} I_n(E). \tag{5.2}$$

Here, the factor A is an adjustable parameter to get the best fit to the observed spectrum.

In Figs. 3–7 we present synthetic electron spectra for Li-, Be-, and B-like sulfur ions over a narrow region of electron energy up to 2.6 eV. It should be noted that the real calculated number of states in Figs. 3–7 is much larger than the number of states included in the Tables. To limit the size of those Tables we list only those with the largest A_a rates. We also compute data for states with Auger electron energy larger than 2.6 eV because they are in one complex and differ only by intermediate moment. Let us explain, for example, how to prepare results for the $1s^22s2p(^3P)nl\,LSJ$ states given in Table V. States with the singlet intermediate moment ^1P are also autoionizing relative to the $1s^22s^2\,^1S$ threshold but they are 20 eV higher from threshold than states with the triplet intermediate moment ^3P, $1s^22s2p(^3P)nl\,LSJ$. We did not include the $1s^22s2p(^1P)nl\,LSJ$ states in our synthetic spectra.

The synthetic spectra for Li-like S^{13+} ions, as presented in Fig. 3, are found to distribute over a very narrow interval of 0.7–0.8 eV for the $[1s2p(^1P)15l\,LSJ-1s2s\ ^1S_0]$ decays and in two more wider intervals of 0.8–1.1 eV and 1.5–1.8 eV for the $[1s2p(^3P)13l\,LSJ-1s2s\ ^3S_1]$ decays, respectively.

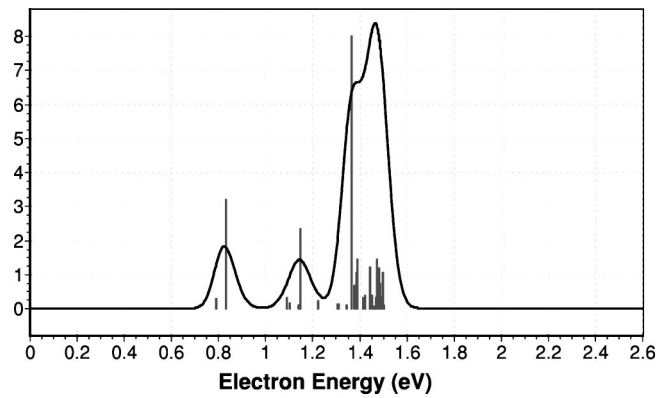

FIG. 4. Synthetic spectrum of S^{12+} with a resolution of 0.1 eV: $[1s^22p9l-1s^22s]$ decay. The scale in the ordinate is in units of $10^{13}\ s^{-1}$.

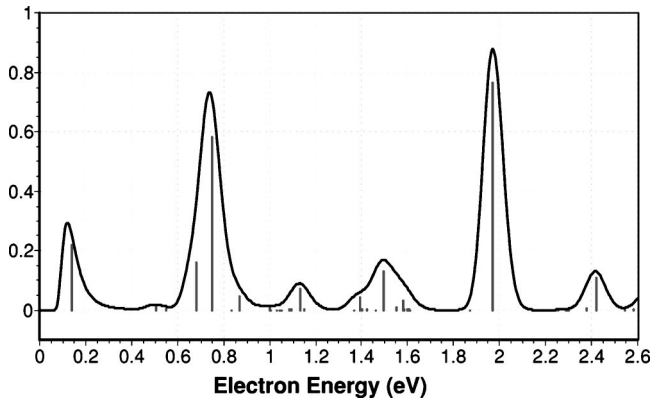

FIG. 5. Synthetic spectrum of S^{11+} with a resolution of 0.1 eV: $[1s^22s2p9l-1s^22s^2]$ decay. The scale in the ordinate is in units of $10^{13}\ s^{-1}$.

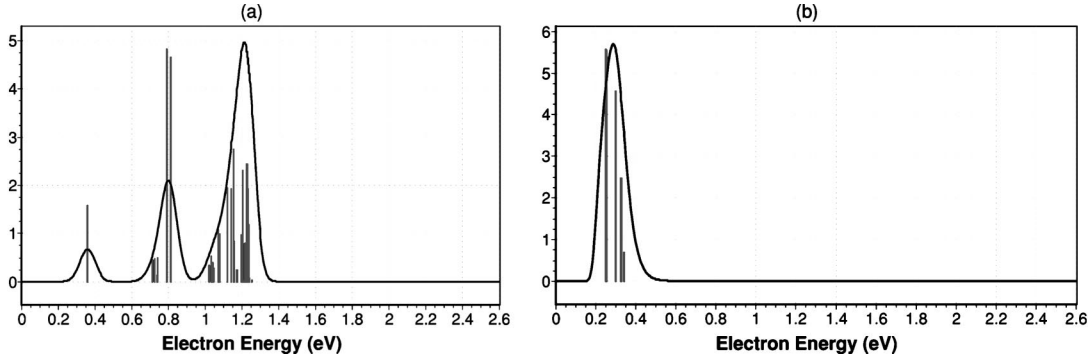

FIG. 6. Synthetic spectrum of S^{11+} with a resolution of 0.1 eV; (a) $[1s^22p^2(^1D)9l-1s^22s2p\,^1P]$ decay and (b) $[1s^22p^2(^1S)7l-1s^22s2p\,^1P]$ decay. The scale in the ordinate is in units of 10^{13} s^{-1}.

In Fig. 4 we demonstrate the synthetic spectrum from the $[1s^22p9l\,LSJ-1s^22s\,^2S_{1/2}]$ decays in Be-like S^{12+} ions. It can be seen from this figure that S^{12+} spectrum consists from three peaks over the energy interval of 0.7–1.6 eV. It is noted that in this energy interval, there are also three peaks from S^{13+} ions though relative intensities of these three peaks are different, as shown in Fig. 3. In this case, the combined $[S^{12+}+S^{13+}]$ spectrum is not much different from S^{12+} spectrum when they are included with equal weights.

Five peaks due to the $[1s^22s2p(^3P)9l\,LSJ-1s^22s^2\,^1S_0]$ decays in synthetic spectrum from B-like S^{11+} ions are present over the interval of 0–2.2 eV, as seen from Fig. 5.

In Figs. 6(a) and 6(b) we present synthetic spectra created from $[1s^22p^2(^1D)9l\,LSJ-1s^22s2p\,^1P_1]$ and $[1s^22p^2(^1S)7l\,LSJ-1s^22s2p\,^1P_1]$ decays, respectively, in S^{11+} ions. Both spectra show peaks distributed over a very narrow range of 0.3–1.25 eV and 0.2–0.4 eV.

We show in Figs. 7(a), 7(b), and 7(c) three synthetic spectra created from single autoionizing states, $1s^22p^2(^3P)7l\,LSJ$, but with three different thresholds of $1s^22s2p\,^3P_J$, $J=0$, 1, and 2. It can be seen from these figures that the energy spectral distributions get narrower as J increases. When $J=0$ [Fig. 7(a)], seven peaks of $[1s^22p^2(^3P)7l\,LSJ-1s^22s2p\,^3P_J]$ decays distribute over the whole 0–2.6 eV energy range. There are only two peaks for $[1s^22p^2(^3P)7l\,LSJ-1s^22s2p\,^3P_J]$ decays with $J=2$ [Fig. 7(c)]. We combine together all three spectra with equal weight, as shown in Fig. 7(d).

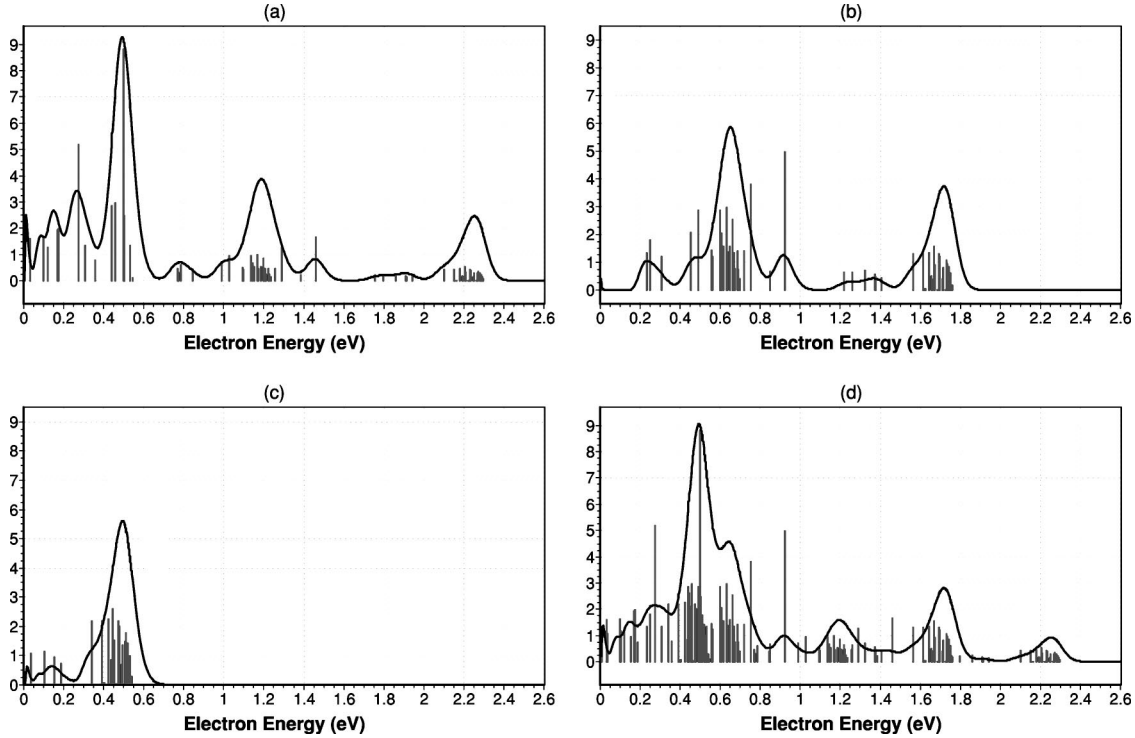

FIG. 7. Synthetic spectrum of S^{11+} with resolution of 0.1 eV; (a) $[1s^22p^2(^3P)7l-1s^22s2p\,^3P_0]$ decay and (b) $[1s^22p^2(^3P)7l-1s^22s2p\,^3P_1]$ decay, (c) $[1s^22p^2(^3P)7l-1s^22s2p\,^3P_2]$ decay, and (d) $[1s^22p^2(^3P)7l-1s^22s2p\,^3P_J]$ decay. The scale in the ordinate is in units of 10^{13} s^{-1}.

VI. COMPARISON OF OBSERVED AND SYNTHETIC SPECTRA

Now we can compare the observed spectra with the synthetic spectra for different charge state ions mentioned above. To understand and explain the observed electron spectra, we need to have the following information and data: (1) the cross sections for forming particular autoionizing states during collisions; (2) the transition energy of electrons emitted; and (3) the autoionization rates from these states. As shown above, reasonably reliable transition energy and autoionization rates can be obtained. On the other hand, there is no simple means to get the cross sections under heavy ion-atom collisions. Under such conditions, we can infer the contribution from different decay channels through comparison of the observed and synthetic electron spectra, only based upon the calculated autoionization rates.

A. He gas target

In Fig. 8(a), the observed electron spectrum from 64 MeV S^{12+} ions colliding with the He gas target is shown with solid dots, meanwhile the synthetic spectrum from the $[1s^22s2p(^3P)9l\,LSJ{-}1s^22s^2\,^1S_0]$ decays of S^{11+} ions is shown with a solid curve (shifted by 0.13 eV from calculated values). It is easily noted that in both spectra there are three peaks at around the 0.3, 1.0, and 2.0 eV regions over the present energy range measured. General features of the observed spectrum are reproduced fairly well with the synthetic spectrum. But it is also noted that the observed spectrum is much broader than the synthetic spectrum, suggesting that there is more significant contributions from other decays.

It is important to note that the present collisions with a dilute He target can be considered (simply) so-called single collisions and means that the charge state of most of projectile ions does not change during passage through the gas target.

To get better agreement between the observed and synthetic spectra, we clearly need to add some other decay channels, with different weighing factors, from similar $1s^22p^2(^1D)9l$ [Fig. 6(a)], $1s^22p^2(^1S)7l$ [Fig. 6(b)], and $1s^22p^2(^3P)7l$ [Fig. 7(d)] of S^{11+} ions. It should be noted that all these $(2l2l')$ states dominantly are formed through the mixing between $2s$ and $2p$ states, followed by one-electron capture into Rydberg states. The combined spectrum of these decays with the previous $1s^22s2p(^3P)9l$ [shown in Fig. 8(a) based upon Fig. 5] decays seems to reproduce the observed spectrum much better [see Fig. 8(b)], except for peaks at 1.0 and 1.8 eV which have been found to be reasonably represented only by adding the contribution of $1s2p15l$ [Fig. 3(a)] and $1s2p13l$ [Fig. 3(b)] decays of S^{13+} ions. The final synthetic spectrum is shown and compared with the observed spectrum in Fig. 8(c). So far this shows much better agreement with the observed spectrum, though there is some chance for further improvement by adding others.

Yet there is a puzzling question: Why do these $1s2p13l$ states of S^{13+} ions contribute to the electron spectrum produced in S^{12+} ion collisions? To form the $1s2p$ core ion, one of the $1s$ electron in the incident S^{12+} ion has to be excited

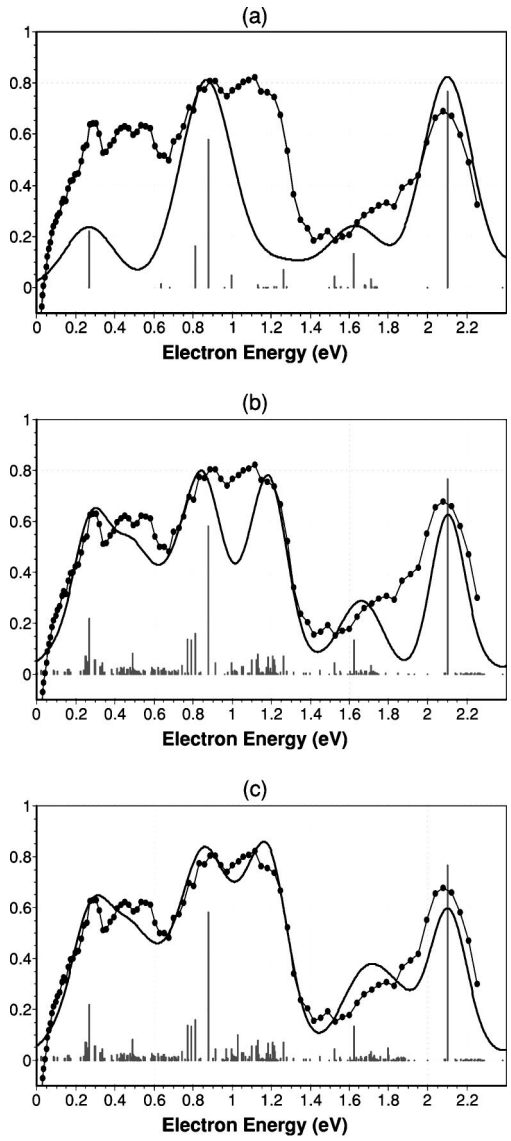

FIG. 8. Electron spectra from $S^{12+}+$He collisions and synthetic spectra: (a) $1s^22s2p9l{-}1s^22s^2$ decay with resolution of 0.3 eV; (b) $\Sigma_i I_i \times$calculated intensity: $I_i=1$ for $i=[1s^22s2p9l{-}1s^22s^2]$, $I_i=1/35$ for $i=[1s^22p^2(^1D)9l{-}1s^22s2p\,^1P]$, $I_i=1/80$ for $i=[1s^22p^2(^1S)7l{-}1s^22s2p\,^1P]$, and $I_i=1/110$ for $i=[1s^22p^2(^3P)7l{-}1s^22s2p\,^3P_J]$ decays with the resolution of 0.2 eV; (c) additional to (b) $I_i=1/30$ for $i=[1s2p(^1P)15l{-}1s2s\,^1S]$ and $I_i=1/20$ for $i=[1s2p(^3P)13l{-}1s2s\,^3S]$ decays with a resolution of 0.2 eV. The solid circles represent the observed data points (see Fig. 1) and the vertical bars the autoionizing rates.

or ionized but such probabilities are expected to be quite small due to a large binding energy ($\sim$3500 eV), although S^{14+} is expected to be appreciable inside the foil at the present collision energy [11]. There is another possibility of the contribution of S^{13+} ions, namely, some role of the metastable $(1s2s)$ S^{14+} ions which are formed during collisions with the He gas target. In fact, it is known for quite sometime that a significant fraction ($\sim$30%) of the metastable state ions are formed after passing through thin foils. Recently it has been experimentally confirmed that similar fractions of the metastable state ions also can be formed even in the He

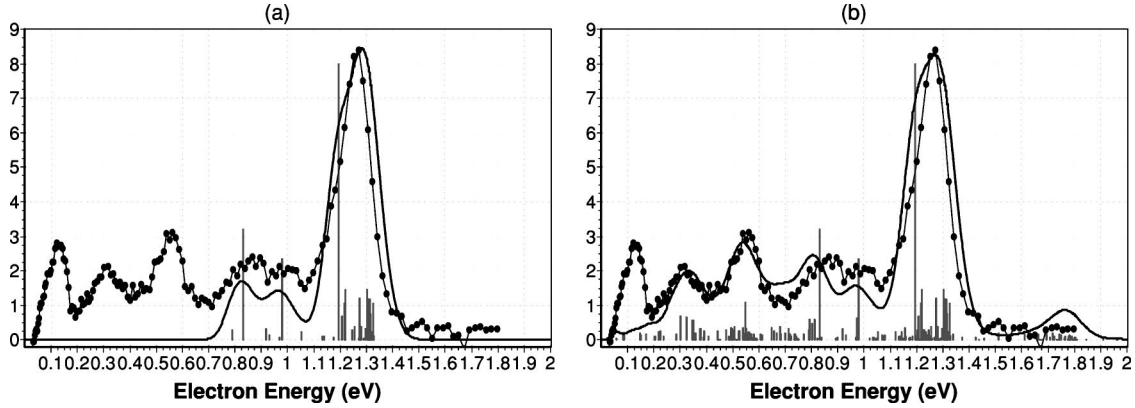

FIG. 9. The observed electron spectra from S^{12+} + C (foil) collisions and synthetic spectra of pure S^{12+} (a) and combined S^{12+} + (1/8)S^{11+} ions with a resolution of 0.12 eV. The captions are the same as in Fig. 8.

gas target [12]. Though presently we do not have quantitative information on the fraction of such metastable state beams of S ions at the present collision energy, the metastable state ions can easily form $1s2p$ state through a mixing between $2s$ and $2p$ states and then capture an electron into their Rydberg state, resulting in $1s2pnl$ states. Thus even a small fraction of this metastable ion beam can play a role in forming such Rydberg state ions.

Furthermore, we should point out why practically no $1s^22p9l$ decay of S^{12+} ions (Fig. 4) contributes to the electron spectrum observed here. To form these states, we need first to remove one of the initial $2s$ electrons (the binding energy of $\sim$450 eV) via either excitation or ionization, accompanied with an electron capture into Rydberg ($9l$) state. Unfortunately no reliable information of the cross sections on formation of such states is available but they are expected to be small, compared with those for forming the core ion $1s^22l2l'$ states which are formed via the efficient mixing between $2l$ and $2l'$ states. Also as the most dominant decay peaks from these states of S^{12+} ions are located at 1.6 eV (see Fig. 4) where the intensities of the observed spectrum are minimum, it can be concluded that the contribution of S^{12+} ions is minor in the present electron energy range.

B. Carbon foil target

In Fig. 9(a) are shown the observed electron spectrum originated from 64 MeV S^{12+} ions in collisions with 2.2 μg/cm^2 thick carbon foil, together with the synthetic spectrum for S^{12+} ions (see Fig. 4). A large portion of the observed spectrum over 0.7–1.8 eV is reproduced nicely, with the calculated energy for the even-parity states of these decays shifted by 0.17 eV, but significant discrepancy is seen at a lower energy region. If the contribution of 1/8 of the intensities of calculated spectra from S^{11+} ions including $[1s^22p^2(^1D)9l\,LSJ{-}1s^22s2p\,^1P_1]$ [Fig. 6(a)], $[1s^22p^2(^1S)7l\,LSJ{-}1s^22s2p\,^1P_1]$ [Fig. 6(b)], and $[1s^22p^2(^3P)7l\,LSJ{-}1s^22s2p\,^3P_J]$ [Fig. 7(d)] decays are added, much better agreement has been obtained over a wide range of the electron energy [see Fig. 9(b)]. Indeed, good agreement is seen over the whole energy range measured, except for a peak at the lowest energy. To get better fitting, we have to shift the last two decay groups [Fig. 6(b) and 7(d)] by +0.05 eV. This small shift required suggests that the present calculations are quite precise and its accuracy is estimated to be within 0.0088% at 565 eV.

While the projectile ions pass through foils, they easily get charge equilibrated and at the present energy the charge distributions of S ions after (not inside) foils are estimated to be roughly 30% of S^{13+} and S^{12+} and 15% of S^{14+} and S^{11+} ions (see [11]). The emitted electron spectrum should be strongly correlated with the charge state upon leaving foils. Indeed the contributions from S^{13+} and S^{14+} ions to the emitted electrons are relatively minor as their autoionization rates are small, as shown in Table III. On the other hand, it is natural that the contribution from S^{12+} ions is dominant with only a small contribution of S^{11+} ions. The present results may suggest that the ion charge distributions after collisions with foil target have to be taken into account to get the best agreement between the observed and synthetic electron spectra.

It is generally believed that, when ions pass through thin foils, a Rydberg state electron is formed through the capture of electrons ''entrained'' to the strong Coulomb field of the incident projectile ions but not of electrons of the target atoms just when the ion leaves the foil surfaces [13].

As mentioned above, the present analysis of the observed Rydberg electron spectra shows the dominance of the $1s^22p9l$ (consisting of $1s^22p$ core ion and $9l$ Rydberg electron) decays of S^{12+} ions (Fig. 4), with small contribution (1/8) of the $1s^22l2l'7l$ ($1s^22l2l'$ core ion and $7l$ Rydberg electron) decays of S^{11+} ions at low energy part. Under the ''entrained'' electron model where the Rydberg electron is attached only when the ion leaves foils, the present result suggests that the average core ion charge ''inside'' foils is 12.9 ± 0.4, which can be compared with the equilibrium charge of 12.5 ''after'' foils taken from the empirical formula [11]. Our preliminary analysis of the Rydberg electron spectrum from 56 MeV Si ions from thin foils [14] also shows that the core ion charge inside foils is about 11.2 ± 0.4, compared with that (11.8) after foils [11]. These results seem to suggest that the ''core charge'' of ions inside foils is not very much different from and, in fact, very similar to the equilibrium charge of ions after foils. This is the first time to

experimentally show the ion charge inside foils, though this is relevant only to the ions which emit the Rydberg electrons.

It should be noted that the incident S^{12+} ion charge in the present paper is close to the expected equilibrium charge after foils [11] and thus the charge equilibration of ions is immediately established once the ions start to penetrate foils. Indeed the observed electron spectra and intensities from the incident S^{12+} ion collisions do not change even if the foil thickness increases from 1.5 to 10 $\mu g/cm^2$ [14].

Of course as the present observed results have been obtained only from a few particular collision systems under limited conditions, the present conclusion on the ion charge distributions observed through the Rydberg electrons should not be generalized to other cases yet. Still we need to investigate similar effects in different collision conditions before getting the definite conclusion on the charge distributions inside foils. Yet we have demonstrated that we can get some reliable information on the charge inside foils through the careful analysis of the Rydberg electrons emitted from foils.

VII. CONCLUSION

In the present paper, we have clearly shown that the observed Coster-Kronig transition electron spectra produced in high-energy S ions in collisions with gas as well as foil target can be synthesized nicely by taking into account the ion charge distributions at the time ions emit these electrons. It has been found that the observed electron spectra are strongly correlated with the equilibrated charge distributions.

We have shown that the average charge of the core ions ''inside'' foils can be inferred from the present analysis of the Rydberg electron spectrum and found to be very similar to the ''after'' foils. It also should be pointed out that we need to have reliable cross sections for forming the autoionization states under heavy-ion collisions to get a better understanding of electron emission mechanisms and better reproduce the observed electron spectrum.

It would be interesting to systematically extend similar electron measurements to different collision energies and different gas targets as the charge equilibrium distributions change, resulting in different electron spectra.

ACKNOWLEDGMENTS

H.T. was supported (in part) by the Chemical Sciences, Geosciences and Biosciences Division, Office of Basic Energy Science, Office of Science, U.S. Department of Energy. U.I.S. acknowledges partial support by Grant No. B503968 from LLNL and the JAERI Foreign Researcher Inviting Program.

[1] I. Yu. Tolstikhina, H. Tawara, U. I. Safronova, M. Imai, M. Sataka, K. Kawatsura, K. Komaki, and Y. Yamazaki, Phys. Scr. **54**, 188 (1996).

[2] K. Kawatsura, M. Sataka, M. Imai, Y. Yamazaki, K. Kuroki, Y. Kanai, S. Arai, and N. Stolterfoht, Nucl. Instrum. Methods Phys. Res. B **124**, 381 (1997).

[3] C. D. Theodosiou, M. Inokuti, and S. T. Manson, At. Data Nucl. Data Tables **35**, 473 (1986).

[4] U. I. Safronova and V. S. Senashenko, *Theory of Spectra of Multicharged Ions* (Energoatomizdat, Moscow, 1984).

[5] M. S. Safronova, U. I. Safronova, N. Nakamura, and S. Ohtani, Phys. Scr. **53**, 689 (1996).

[6] R. D. Cowan, *The Theory of Atomic Structure and Spectra* (University of California Press, Berkeley, CA, 1981).

[7] K. Kawatsura, M. Sataka, H. Naramoto, M. Imai, Y. Yamazaki, K. Kuroki, Y. Kanai, T. Kambara, Y. Awaya, J. E. Hansen, I. Kadar, and N. Stolterfoht, Nucl. Instrum. Methods Phys. Res. B **53**, 421 (1991).

[8] M. S. Pindzola, T. W. Gorczyca, N. R. Badnell, D. C. Griffin, M. Stenke, G. Hofmann, B. Weissbecker, K. Tinschert, E. Salzborn, A. Müller, and G. H. Dunn, Phys. Rev. A **49**, 933 (1994).

[9] U. I. Safronova and T. Kato, Phys. Scr. **53**, 461 (1996).

[10] L. A. Vainshtein and U. I. Safronova, Phys. Scr. **31**, 519 (1985).

[11] K. Shima, N. Kuno, M. Yamanouchi, and H. Tawara, At. Data Nucl. Data Tables **51**, 173 (1992).

[12] M. Zamkov, H. Aliabadi, E. P. Benis, P. Richard, H. Tawara, and T. J. M. Zouros, Phys. Rev. A **64**, 052702 (2001).

[13] J. Burgdoerfer and C. Bottcher, Phys. Rev. Lett. **61**, 2917 (1988).

[14] M. Imai, M. Sataka, S. Kitazawa, K. Komaki, K. Kawatsura, H. Shibata, H. Tawara, T. Azuma, Y. Kanai, and Y. Yamazaki, Nucl. Instrum. Methods Phys. Res. B (to be published).